Iron Loss Reduction in Permanent Magnet Synchronous Motor by Using Stator Core Made of Nanocrystalline Magnetic Material

Nicolas Denis[1], Masaki Inoue[2], Keisuke Fujisaki[1], Hiromitsu Itabashi[3], and Tomoaki Yano[4]

[1]Toyota Technological Institute, Nagoya 468-8511, Japan
[2]Hitachi Metals, Ltd., Yasugi 692-0014, Japan
[3]Hitachi Metals. Ltd., Tottori 689-1121, Japan
[4]Japan Aerospace Exploration Agency, Sagamihara 252-5210, Japan

This paper presents the results of experimental trials carried out on a permanent magnet synchronous motor (PMSM) that uses a stator core made of a nanocrystalline magnetic material (FINEMET). It is demonstrated that the manufactured stator can reduce the PMSM total iron loss by 64% to 75% compared with an equivalent motor using a stator made of conventional non-oriented silicon steel. The experimental results are confirmed by 2-D finite-element analysis.

***Index Terms*— Amorphous magnetic material (AMM), FINEMET, iron loss, nanocrystalline magnetic material (NMM), permanent magnet synchronous motor (PMSM).**

I. Introduction

PERMANENT magnet synchronous motors (PMSMs) face three main types of losses, which are copper loss, mechanical friction loss, and iron loss. For the sake of sustainable energy consumption, it is vital to reduce the losses in electrical motors. Copper losses and mechanical friction losses can be theoretically reduced to nearly zero by using superconducting materials and magnetic bearings in a vacuum environment, respectively. However, work remains to be done in order to manufacture motor cores with high-performance magnetic materials that can drastically reduce iron losses.

Due to their low cost and simplicity of manufacture, non-oriented (NO) silicon steel sheets are usually used in PMSM cores. Some research studies are focusing on using thin NO sheets in order to reduce eddy currents [1]. However, the potential of iron loss reduction by improving NO steel is limited due to the inherent characteristics of the material. Amorphous magnetic material (AMM) is produced in thin ribbons and has high resistivity and low coercive force compared to NO, thus offering lower iron loss density [2]. AMM has long been used in applications such as transformers [3], but the manufacture of the motor core is more challenging due to its poor mechanical workability. However, the technological advances in amorphous ribbons manufacturing have permitted improvements in surface quality, resulting in higher lamination factor [4]. In addition, new cutting techniques have made the manufacture of electrical motor cores easier [5]–[7].

As a result, numerous manufacture trials can be found in the literature. Since iron losses increase with frequency, AMM has proved to be particularly beneficial to high-speed motors [8], [9]. Moreover, AMM can also be found in several axial-field-type motors made of wound cores that require small amount of material cutting [8], [10]–[12]. However, since axial-field and/or high-speed motors do not suit every application, the development of radial-field-type lower-speed electrical motors has also been tried. Magnetic cores of radial-field-type motors require more cutting, and then manufacturing them using AMM is more difficult. Nevertheless, AMM has been used for the manufacture of the stator core of an induction motor [13] and a reduction in iron loss by about 50% in no-load and sinusoidal-fed supply conditions has been found, compared to the same motor using low-loss silicon steel. AMM has also been used to manufacture the stator of a synchronous reluctance motor [14]. The motor, driven by an inverter in load condition, has shown a reduction in iron loss by 63% at 8500 rpm, compared to the same motor using silicon steel. Finally, the manufacture of a PMSM stator using AMM has resulted in an iron loss reduction by 50% when the PMSM is rotated by an auxiliary motor [15] and by 56% when driven by a pulsewidth modulation (PWM) inverter [16], compared to the same motor using silicon steel only.

Nanocrystalline magnetic material (NMM) is derived from AMM, but its composition differs a little. In addition, while the amorphous material is non-crystalline, NMM is annealed over its crystallization temperature, which then presents very small and uniform grains [17]. This material presents lower iron loss density compared to AMM. Inductor cores made of NMM have exhibited lower iron losses compared to their counterparts made of AMM [18], grain-oriented silicon steel, or high-performance NO silicon steel [19]. A trial manufacture of a PMSM stator core with NANOMET-type NMM is reported in [20]. The experimental results show a motor iron loss reduction of about 70%. In this paper, a stator core manufactured using FINEMET-type NMM is presented and used as part of a PMSM. FINEMET and NANOMET are both nanocrystalline, but their respective compositions slightly differ. Compared to NANOMET, the FINEMET ribbon is thinner, which can not only decrease the eddy currents but also make the manufacture more difficult. It not only has lower magnetic flux density saturation but also has lower coercive force. Concerning the material-specific iron losses, the data provided in [20] are for

Manuscript received March 9, 2017; revised April 21, 2017; accepted April 27, 2017. Date of publication May 2, 2017; date of current version October 24, 2017. Corresponding author: N. Denis (e-mail: nicolas.denis@toyota-ti.ac.jp).

Color versions of one or more of the figures in this paper are available online at http://ieeexplore.ieee.org.

Digital Object Identifier 10.1109/TMAG.2017.2700471

TABLE I
MAGNETIC MATERIAL CHARACTERISTICS

Material type	NMM	NO
Composition	Fe-Si-B-Cu-Nb	Fe-Si
Thickness (μm)	18	350
Saturation magnetic flux density (T)	1.23	2.12
Resistivity (μΩ·m)	1.20	0.52
Coercive force (A/m)	2.5	50

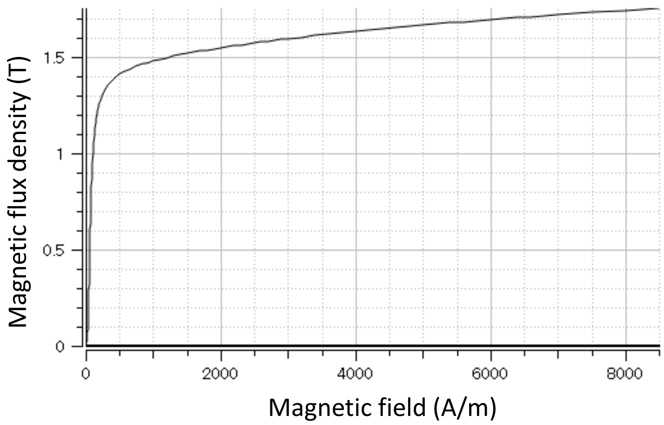

Fig. 1. *B–H* curve of 35H300.

a a magnetic flux density of 1.5 T only, which is a value that cannot be reached in the FINEMET. Consequently, a fair comparison is not possible. Experimental trials are carried out to evaluate the potential iron loss reduction compared to an equivalent motor using a stator made of NO silicon steel. Section II presents the magnetic material characteristics along with the motor geometry and explanations about the NMM stator manufacture. Section III explains the experimental protocol for the evaluation of the PMSM iron losses and provides the experimental results. Section IV details the 2-D finite-element analysis (FEA) and provides the numerical calculation results.

II. MAGNETIC MATERIAL CHARACTERISTICS AND MOTOR GEOMETRY

A. Magnetic Material Characteristics

The NMM used in this paper is the FINEMET developed by the Hitachi Metals, Ltd. [21]. Moreover, the conventional NO silicon steel 35H300 is used for comparison. The characteristics of these two materials are given in Table I. The *B–H* curves of both materials are given in Figs. 1 and 2. The iron loss density characteristics of both materials are given in Figs. 3 and 4. The characteristics of the NMM have been measured using a *B–H* analyzer, while those of the 35H300 come from the manufacturer's information.

B. Motor Geometry

The motor used in this paper is a PMSM with 8 poles and 12 slots. The NdFeB sintered magnets are buried inside the rotor. The cross section of the motor is illustrated in Fig. 5, and Table II gives the motor dimensions. In this paper,

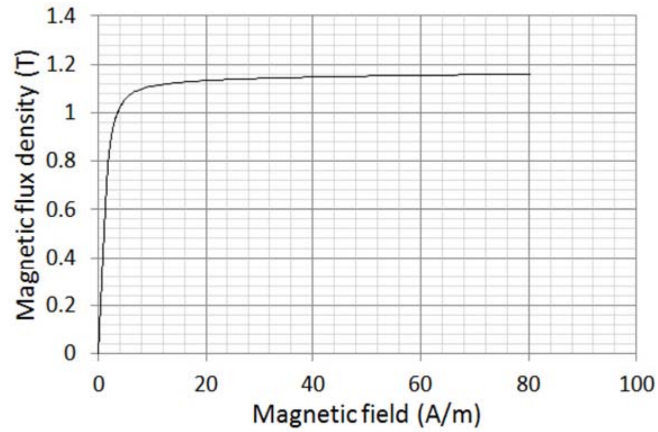

Fig. 2. *B–H* curve of NMM.

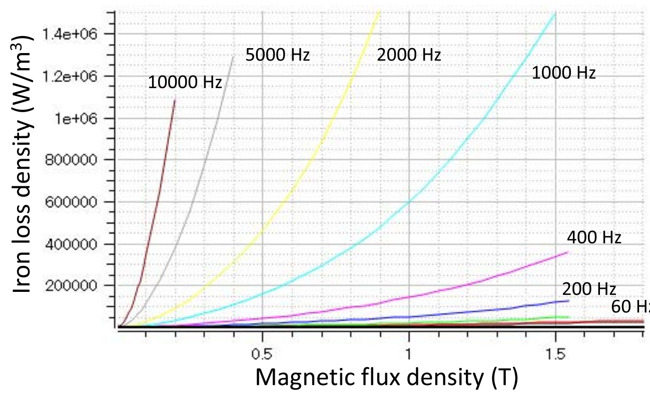

Fig. 3. Iron loss density characteristic of 35H300.

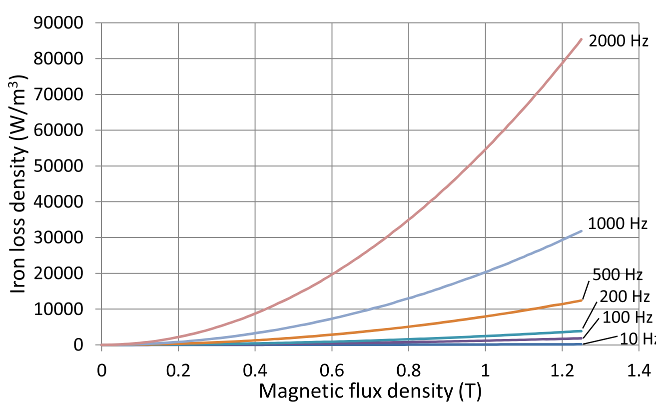

Fig. 4. Iron loss density characteristic of NMM.

two different motors are tested. They are identical except for the stator material. The first, called NO-PMSM, has a stator made of 35H300 silicon steel sheets, and the second, called NMM-PMSM, has a stator made of stacked NMM sheets. It should be noted that both motors have a rotor made of 35H300.

C. Manufacture of NMM Stator

The maximum width of the NMM ribbon that can be produced for the time being is 63 mm. Since the stator diameter is 128 mm, it is manufactured in four separate pieces.

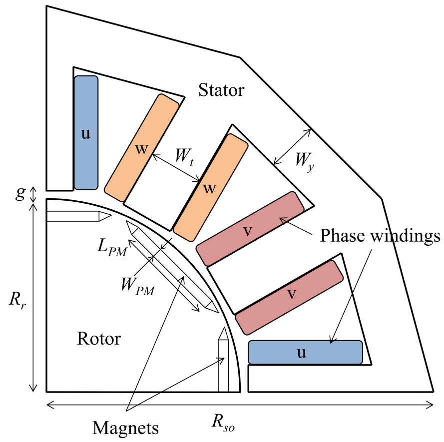

Fig. 5. Quarter cross section of the PMSM.

TABLE II
PMSM GEOMETRICAL DIMENSIONS

Radius of stator core R_{so}	64 mm
Radius of rotor core R_r	37 mm
Air gap g	1.25 mm
Yoke width W_y	9.2 mm
Tooth width W_t	10 mm
Magnet length L_{PM}	20 mm
Magnet thickness W_{PM}	2 mm
Axial length	47 mm

The first step consists in cutting the ribbon in rectangular sheets and piling them up to obtain a laminated stack; then, an annealing process at about 550 °C is performed in order to improve the magnetic properties. A resin impregnation step is then necessary in order to obtain electrical isolation in the interlaminations. The laminated stack is then cut in the shape of the stator core using electric discharge machining. Finally, an etching process is performed in order to increase the electrical resistivity of the stator edge faces that have locally melted during the cutting step. Another possibility would have been to perform electric discharge machining before lamination, as in [20], but this procedure would have been quite longer and more complex considering the thinness of the ribbon. The obtained four pieces are shown together in Fig. 6. It should be noted that the thinness of the NMM ribbon and the specific manufacture process result in a stator with a space factor of 81%, while the stator made of 35H300 reaches a space factor of 99%. The pieces are then inserted into the motor casing, as illustrated in Fig. 7. The rotor is mounted afterward.

III. EXPERIMENTAL TESTS

A. Methodology

The NO-PMSM and NMM-PMSM total iron losses are measured under what is called no-current condition in this paper. It is different from the conditions in [20], where the motor is driven by a PWM inverter, but is still thought to be a simple way to get a good evaluation of the potential iron loss reduction. The experimental test bench is illustrated in Fig. 8. The PMSM is rotated using an external brushless dc (BLDC)

Fig. 6. NMM stator core manufactured in four pieces.

Fig. 7. NMM stator core inserted into the motor casing.

motor and its windings are left in open circuit. The BLDC motor output mechanical power compensates for the force needed to drive the PMSM rotor at a given speed. This resistance force is caused by the PMSM mechanical friction P_f and its iron losses P_i that are solely due to the rotation of the rotor magnets. Here, P_i is considered to be the sum of the iron losses in the rotor, stator, and magnets. A torque meter is connected between the two motors in order to measure the BLDC motor output torque T_{mes} (in N · m) and the rotational speed ω (rad/s). It is then possible to write

$$\omega T_{\text{mes}} = P_i + P_f. \tag{1}$$

The maximum torque measurable by the torque meter is 1 N · m and its accuracy is ±0.002 N · m.

Performing the measurements as explained in (1), it is impossible to distinguish P_i from P_f. Consequently, a subsequent measurement is done to measure P_f only, which is due to the friction in the rotor bearings and the friction of air. This measurement consists in using the same test bench as in Fig. 8 but replacing the PMSM rotor by a rotor with demagnetized magnets; the shape and bearings are identical. The term P_i then disappears in (1), making it possible to measure P_f.

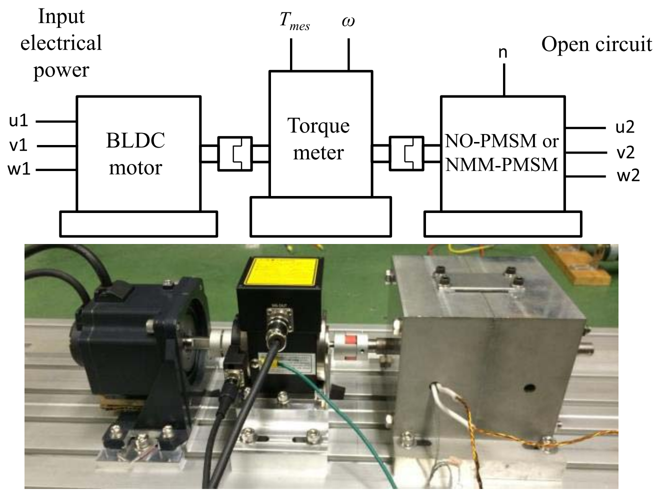

Fig. 8. Experimental bench for test in no-current condition.

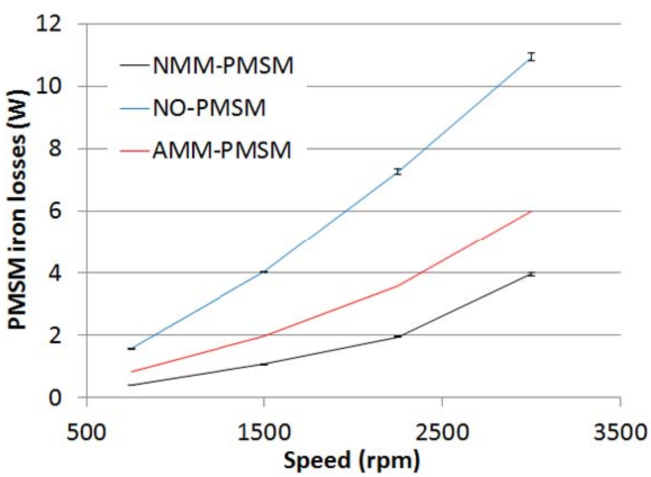

Fig. 9. Measurement results.

B. Measurements Results

The measurements have been done at 750, 1500, 2250, and 3000 rpm. First of all, the motor is rotated at the desired speed for about 30 min to warm up. Then T_{mes} and ω are measured for 20 s with a measurement rate of 1 s. The measurements over the 20 s time span are then averaged. The above procedure is repeated ten times, excluding the warm up that is done only once. For a given speed, the average and standard deviation of the ten obtained values are calculated. The results are presented in the graph of Fig. 9, in which the standard deviation is illustrated by bars. It should be noted that the torque meter accuracy given in the previous section means that the accuracy of the measured mechanical power ωT_{mes} is equal to ± 0.157 W at 750 rpm and ± 0.628 W at 3000 rpm. Fig. 9 also includes the results obtained with a stator made of AMM, which have already been presented in [15]. Using the AMM stator, an average iron loss reduction of about 50% is obtained compared to the NO-PMSM. Using the NMM stator, an average reduction of about 70% is obtained, which is very similar to that reported in [20].

IV. Numerical Analysis by Finite-Element Method

A. 2-D Numerical Model and Iron Loss Calculation Method

The purpose of this section is to confirm the experimental data by numerical analysis using a rather simple model. Consequently, some assumptions are considered and simplifications are done and detailed below.

Time-stepping 2-D FEA is chosen for the numerical analysis. The number of elements of the 2-D finite-element mesh is 28 964. For the magnetic field analysis, the following 2-D A-method equation is used:

$$\frac{\partial}{\partial x}\left(\nu_y \frac{\partial A_z}{\partial x}\right) + \frac{\partial}{\partial y}\left(\nu_x \frac{\partial A_z}{\partial y}\right) = -J_0 + \sigma \frac{\partial A_z}{\partial t} \qquad (2)$$

where A_z is the vector potential on the z-axis, ν_x and ν_y are the magnetic reluctance on the x- and y-axes, J_0 is the current density supplied to the coil parts, and σ is the electrical conductivity of the material. Since both NMM and NO materials are considered quasi-isotropic, ν_x and ν_y are taken equal and are derived from the B–H curves of Fig. 1 or 2. In accordance with the test conditions explained in Section III, J_0 is taken to be equal to zero.

Finally, as will be detailed later in this section, the eddy currents in the stator and rotor parts are not calculated and the eddy current losses are approximated using the Steinmetz equations. Consequently, σ is taken to be null in the rotor and stator. However, the electrical conductivity of the magnets is considered ($\sigma_m = 6.25 \times 10^5$ S/m) and their eddy currents are calculated.

In order to evaluate the iron loss density in a given element of the stator or rotor, the magnetic flux density calculated using (2) is first decomposed into its radial and tangential components B_r and B_t, respectively. A fast Fourier transform (FFT) is then performed to find the harmonic components of B_r and B_t. The hysteresis and eddy current loss density in the element are then calculated using the Steinmetz approximation [22]

$$W_{s,t} = \sum_{i=1}^{N_h} \left(K_{\mathrm{hys},i}\left(B_{t,i}^2 + B_{r,i}^2\right) f_i + K_{\mathrm{ed},i}\left(B_{t,i}^2 + B_{r,i}^2\right) f_i^2\right) \qquad (3)$$

where i is the harmonic rank, N_h is the rank of the highest harmonic, f_i is the frequency of the ith harmonic, and $B_{r,i}$ and $B_{t,i}$ are the amplitudes of the ith harmonic of B_r and B_t, respectively. $K_{\mathrm{hys},i}$ and $K_{\mathrm{ed},i}$ are the hysteresis and eddy current loss Steinmetz constants, respectively, which depend on the frequency and are obtained from the characteristics shown in Figs. 3 and 4.

It should be noted that the iron loss calculation in (3) does not consider the impact of magnetic flux rotation that increases the losses compared to the case of an unidimensional one [23]. Moreover, the hysteresis loss calculation in (3) considers the harmonics of the magnetic flux density, but some authors point out that hysteresis losses are actually independent of the flux density wave shape (and therefore independent of the harmonic content) unless minor loops occur [24]. Finally, the calculation does not take into account the effect of mechanical stress on the material iron loss density [25]. Mechanical stress can occur

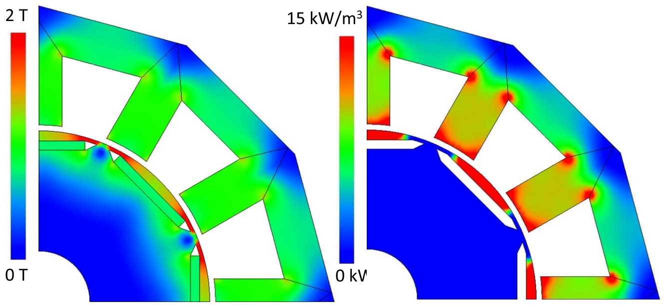

Fig. 10. Peak magnetic flux distribution (left) and iron loss density distribution (right) of the NO-PMSM at 750 rpm.

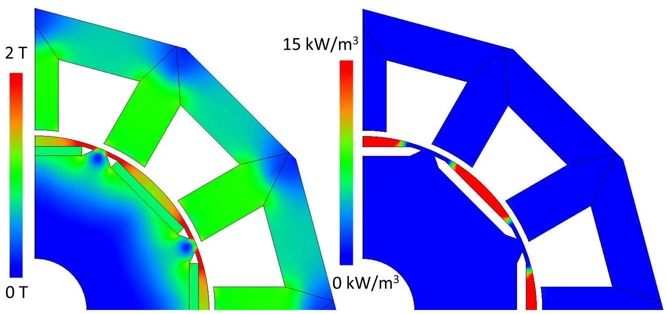

Fig. 11. Peak magnetic flux distribution (left) and iron loss density distribution (right) of the NMM-PMSM at 750 rpm.

during the cutting process or if compressive forces are applied when mounting the stator into the casing. Even though the model proposed here contains simplifications and assumptions, it has proved to provide relatively satisfying agreement with experiment results in the case of NO silicon steel [15], [22] and is considered sufficient here given the purpose of this paper.

The magnetic field analysis allows calculating the eddy current density J_s in each mesh element of the magnets. The magnet eddy current loss in a given element is then calculated by Ohm's law and time average

$$W_m = \frac{1}{T_e}\sum_{k=1}^{N_t}\frac{J_s^2(k)}{\sigma_m}dt \tag{4}$$

where N_t is the number of time samples of the numerical simulation, T_e is the electrical period, and dt is the time sampling duration.

B. Numerical Calculation Results

The distributions of the peak maximum magnetic flux density and the iron loss density of NO-PMSM and NMM-PMSM are presented in Figs. 10 and 11, respectively. Figs. 10 and 11 illustrate the case of 750 rpm rotational speed. The magnetic flux density distributions of the stator appear similar, but it is possible to notice a decrease in the NMM stator compared to the NO stator. This is thought to be due to the lowest magnetic flux density saturation level of the NMM. The iron loss density distributions present the iron losses in the stator and rotor only since the magnet eddy currents are calculated at a different step and cannot be shown together. A similar distribution is observed in the rotor while a large decrease appears in the stator.

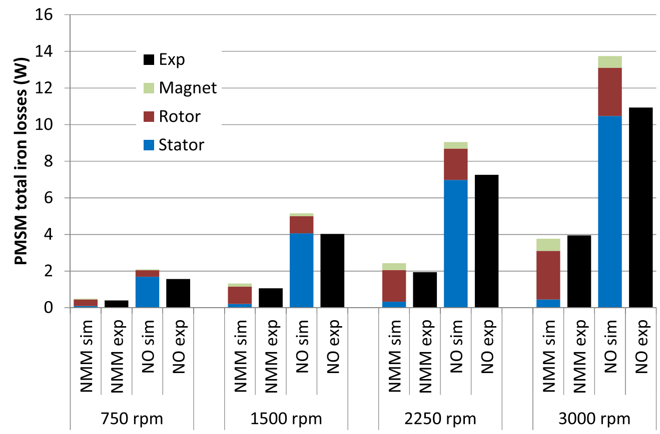

Fig. 12. Total iron losses of NO-PMSM and NMM-PMSM (simulation results and experimental data).

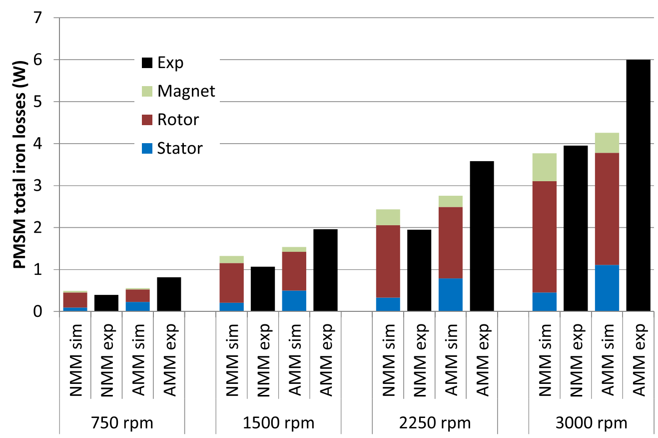

Fig. 13. Total iron losses of AMM-PMSM and NMM-PMSM (simulation results and experimental data).

The calculation results of the total iron losses of both NO-PMSM and NMM-PMSM are illustrated in Fig. 12 along with the experimental results. The discrepancies between the calculation and the experimental results stay reasonable in spite of the approximations made in the calculation and the accuracy of the measurements. Moreover, it can be seen that the iron loss decrease found by calculation is higher than that found by experiment. As a quantitative example, the decrease in iron losses between the NMM-PMSM and the NO-PMSM at 3000 rpm is found to be 64% by experiment while it is 73% by calculation. In order to explain this, it should be recalled that the cutting technique locally melts the material, which causes short circuits at the edges of the core between sheets. During the etching step, the resistivity of the edge surfaces is increased but stays quite low. This increases the eddy currents compared to the case where the interlamination is perfectly isolated at the core edge. This problem does not appear for the NO stator, but is thought to have a quite large impact on the NMM stator core. However, it is not taken into account in the FEA, which could explain the differences in the iron loss decrease rate.

Similar to Fig. 12, Fig. 13 compares the iron loss data of the NMM-PMSM with the numerical calculation and experimental results of the AMM-PMSM presented in [15]. According to the numerical calculation, the NMM stator iron losses are lower than that of the AMM stator. It can also be seen that the total iron loss reduction found by calculation between the AMM-PMSM and the NMM-PMSM is smaller than that found by experiment. In order to explain this, it should be noted that the manufacture of the AMM stator does not include an etching step, contrary to that of the NMM stator. Consequently, the resistance of the AMM stator edge surfaces is lower than that of the NMM stator, which increases the eddy currents. As stated in the explanation of Fig. 12, this effect is not taken into account in the numerical calculation, hence explaining the difference in loss decrease rate between the numerical calculation and experiments.

V. Conclusion

In this paper, the iron losses of a PMSM using a stator core made of NMM have been measured by experiments and evaluated by 2-D FEA. An iron loss decrease by 64%–75% has been found by experiment. The future works should aim at evaluating the motor performance when driven by a voltage source PWM inverter. This should include the torque capacity as well as the efficiency and the decrease in iron losses.

Acknowledgment

This work was supported by the Ministry of Education, Culture, Sports, Science, and Technology Program, Japan, for private universities.

References

[1] T. A. Huynh and M.-F. Hsieh, "Performance evaluation of thin electrical steels applied to interior permanent magnet motor," in *Proc. 19th ICEMS*, Chiba, Japan, Nov. 2016, pp. 1–6.

[2] H. Fujimori, H. Yoshimoto, T. Masumoto, and T. Mitera, "Anomalous eddy current loss and amorphous magnetic materials with low core loss (invited)," *J. Appl. Phys.*, vol. 52, no. 3, pp. 1893–1898, Mar. 1981.

[3] A. J. Moses, "Demonstration of the feasibility of the use of amorphous magnetic material as transformer core material," in *Proc. 12th Int. Conf. Electr. Distrib.*, Birmingham, U.K., May 1993, pp. 1–3.

[4] R. Hasegawa, "Present status of amorphous soft magnetic alloys," *J. Magn. Magn. Mater.*, vols. 215–216, pp. 240–245, Jun. 2000.

[5] S. R. Ning, J. Gao, and Y. G. Wang, "Review on applications of low loss amorphous metals in motors," *Adv. Mater. Res.*, vols. 129–131, pp. 1366–1371, Aug. 2010.

[6] T. Suzuki, S. Itho, G. Terada, A. Chiba, M. Yoshida, and H. Watanabe, "Electric motor characteristic of SRM that uses heat-treated amorphous alloys accumulating body," (in Japanese), *Inst. Elect. Eng. Jpn.*, vol. 142, RM-03-142, pp. 35–40, 2003.

[7] S. H. Li, Z. C. Lu, D. R. Li, C. W. Lu, and S. X. Zhou, "Investigation on the core loss of amorphous stator core for high-speed motor," *Small Special Electr. Mach.*, no. 6, pp. 24–25, 2009.

[8] Z. Wang, Y. Enomoto, R. Masaki, K. Souma, H. Itabashi, and S. Tanigawa, "Development of a high speed motor using amorphous metal cores," in *Proc. IEEE 8th Int. Conf. Power Electron. ECCE Asia*, May/Jun. 2011, pp. 1940–1945.

[9] R. Kolano, K. Krykowski, A. Kolano-Burian, M. Polak, J. Szynowski, and P. Zackiewicz, "Amorphous soft magnetic materials for the stator of a novel high-speed PMBLDC motor," *IEEE Trans. Magn.*, vol. 49, no. 4, pp. 1367–1371, Apr. 2013.

[10] Z. Wang *et al.*, "Development of a permanent magnet motor utilizing amorphous wound cores," *IEEE Trans. Magn.*, vol. 46, no. 2, pp. 570–573, Feb. 2010.

[11] G. S. Liew, W. L. Soong, N. Ertugrul, and J. Gayler, "Analysis and performance investigation of an axial-field PM motor utilising cut amorphous magnetic material," in *Proc. 20th Australasian Universities Power Eng. Conf.*, Christchurch, New Zealand, Dec. 2010, pp. 1–6.

[12] Z. Wang *et al.*, "Development of an axial gap motor with amorphous metal cores," *IEEE Trans. Ind. Appl.*, vol. 47, no. 3, pp. 1293–1299, May/Jun. 2011.

[13] M. Dems and K. Komeza, "Performance characteristics of a high-speed energy-saving induction motor with an amorphous stator core," *IEEE Trans. Ind. Electron.*, vol. 61, no. 6, pp. 3046–3055, Jun. 2014.

[14] A. Chiba *et al.*, "Test results of an SRM made from a layered block of heat-treated amorphous alloys," *IEEE Trans. Ind. Appl.*, vol. 44, no. 3, pp. 699–706, May 2008.

[15] S. Okamoto, N. Denis, Y. Kato, M. Ieki, and K. Fujisaki, "Core loss reduction of an interior permanent-magnet synchronous motor using amorphous stator core," *IEEE Trans. Ind. Appl.*, vol. 52, no. 3, pp. 2261–2268, May/Jun. 2016.

[16] N. Denis, Y. Kato, M. Ieki, and K. Fujisaki, "Core losses of an inverter-fed permanent magnet synchronous motor with an amorphous stator core under no-load," *AIP Adv.*, vol. 6, p. 055916, Mar. 2016.

[17] Y. Yoshizawa, S. Oguma, and K. Yamauchi, "New Fe-based soft magnetic alloys composed of ultrafine grain structure," *J. Appl. Phys.*, vol. 64, no. 10, pp. 6044–6046, Nov. 1988.

[18] H. Kosai, Z. Turgut, T. Bixel, and J. Scofield, "Performance comparison of Finemet and Metglas tape cores under non-sinusoidal waveforms with DC bias," *IEEE Trans. Magn.*, vol. 52, no. 7, Jul. 2016, Art. no. 8400704.

[19] S. Odawara *et al.*, "Impact of material on the iron losses of a reactor with an air gap," *IEEE Trans. Magn.*, vol. 51, no. 11, Nov. 2015, Art. no. 8401404.

[20] N. Nishiyama, K. Tanimoto, and A. Makino, "Outstanding efficiency in energy conversion for electric motors constructed by nanocrystalline soft magnetic alloy 'NANOMET' cores," *AIP Adv.*, vol. 6, Mar. 2016, p. 055925.

[21] *Amorphous Alloy Ribbon Metglas*, document Catalog HJ-B10-B, Hitachi Metals, Ltd., May 2014.

[22] K. Yamazaki and Y. Seto, "Iron loss analysis of interior permanent-magnet synchronous motors-variation of main loss factors due to driving condition," *IEEE Trans. Ind. Appl.*, vol. 42, no. 4, pp. 1045–1052, Jul./Aug. 2006.

[23] Y. Guo, J. G. Zhu, J. Zhong, H. Lu, and J. X. Jin, "Measurement and modeling of rotational core losses of soft magnetic materials used in electrical machines: A review," *IEEE Trans. Magn.*, vol. 44, no. 2, pp. 279–291, Feb. 2008.

[24] E. Barbisio, F. Fiorillo, and C. Ragusa, "Predicting loss in magnetic steels under arbitrary induction waveform and with minor hysteresis loops," *IEEE Trans. Magn.*, vol. 40, no. 4, pp. 1810–1819, Jul. 2004.

[25] K. Fujisaki and S. Satoh, "Numerical calculations of electromagnetic fields in silicon steel under mechanical stress," *IEEE Trans. Magn.*, vol. 40, no. 4, pp. 1820–1825, Jul. 2004.